Supporting Information

One-step supramolecular co-assembly of lignin into micro-/nanospheres for photostable, sustained-release delivery of photosensitive pesticides

Hong-zhen Sun[a,b], Hai-xiu Bai[c], Yu-han Shang[a], Xin-yao Ye[b], Min Wang[d], Wei Xu[e], Jia-long Wen[b,*], Da-xia Zhang[a,*], Feng Liu[a,*]

[a] College of Plant Protection, Shandong Agricultural University, Tai'an, Shandong, 271018, China

[b] State Key Laboratory of Efficient Production of Forest Resources, Beijing Forestry University, Beijing 100083, China

[c] Shandong Medicine Technician College, Tai'an, Shandong 271018, China

[d] Jinan Tianbang Chemical Co., Ltd., Ji'nan, Shandong, 251600, China

[e] Shandong Shibang Agrochemical Co., Ltd., Heze, Shandong, 274300, China

* Corresponding authors：

(Jia-long Wen) E-mail：wenjialong@bjfu.edu.cn

(Da-xia Zhang) E-mail：daxia586@163.com

(Feng Liu) E-mail：fliu@sdau.edu.cn

Table of contents

5. Movie S1 Introduction

1. Experimental Section

1.1 Materials

Technical-grade lambda-cyhalothrin (LC), abamectin (ABM), and fluazinam (FZN) (purity ≥ 90%) were used as received from the original packaging without further purification or treatment.

1.2 Characterization of EB@MSs and EB@NSs

Solid-state and chemical characterizations were performed on EB@MSs and EB@NSs. The as-prepared 2.3 wt% EB@MSs and EB@NSs suspensions were washed and centrifuged three times; the resulting pellets were dried and gently ground into powders. Pristine EB, pristine SL, and a physically ground EB/SL mixture (EB@SL) were analyzed in parallel as controls. X-ray diffraction (XRD) was collected using Cu Kα radiation over 2θ = 5°-90° at a scan rate of 2° min^{-1}. Thermogravimetric analysis (TGA) was conducted from 0 to 800 °C at 20 °C min^{-1} under a nitrogen atmosphere. For Fourier transform infrared spectroscopy (FTIR), samples were dried at 60 °C, thoroughly ground with KBr, and pressed into pellets for 1 min; spectra were recorded over 4000-400 cm^{-1}. X-ray photoelectron spectroscopy (XPS) was acquired in the standard mode, including a wide-scan survey spectrum and high-resolution core-level scans, using dried powders prepared from the washed EB@MSs pellet together with the above references.

Elemental mapping was conducted by EDS coupled with electron microscopy. Specifically, 0.25 mL of the as-prepared 2.3 wt% EB@MSs or EB@NSs dispersion was diluted with 5 mL deionized water. For EB@MSs, 0.01 mL of the diluted dispersion was spread onto a silicon wafer and dried at room temperature for 24 h prior to SEM-EDS mapping. For EB@NSs, a small aliquot was drop-cast onto a clean copper grid and vacuum-dried at 40 °C before TEM-EDS mapping. Raman spectra of SL, EB, EB@SL, and EB@MSs were collected using a 532 nm laser (1.6 mW) with two accumulations (total integration time: 10 s) over 0-4000 cm^{-1}.

1.3 Characterization of cyclohexanone-induced self-assembly of SL

A 0.1 wt% SL aqueous solution was prepared by dissolving 0.2 g of SL in 19.98 g of purified water. Cyclohexanone was added to the SL solution (0, 0.6, 0.9, 1.2, 1.5, 1.8, 2.4, or 3.0 g) while keeping the total mass of the mixture (0.1 wt% SL solution + cyclohexanone) constant at 20 g. Each sample was transferred to a four-sided transparent cuvette for Tyndall-effect observation under infrared illumination, followed by zeta potential measurements.

To probe solvent-induced changes in the aggregation state of SL, a 3 wt% SL aqueous solution was prepared, and cyclohexanone was added at different dosages to 20 g of the 3 wt% SL solution. After stirring for 10 min, the resulting solids were collected by centrifugation, washed three times, and dried prior to FTIR measurements.

Fluorescence excitation spectra during solvent induction were recorded using a fluorescence spectrophotometer (F-4600, HITACHI). The total mass of each sample was fixed at 20 g, and cyclohexanone was introduced at 0-8% (w/w; 0, 1, 2, 3, 4, 5, 6, 7, and 8%) followed by thorough mixing. Spectra were collected over an excitation range of 200-450 nm at a scan rate of 1200 nm min^{-1} with excitation/emission slit widths of 1/5 nm and a photomultiplier tube voltage of 700 V.

UV-vis absorption spectra of SL solutions during solvent exchange were collected using a NanoDrop One spectrophotometer (Thermo Fisher Scientific). The total mass was fixed at 20 g with SL maintained at 0.1 wt% of the overall mixture, and cyclohexanone was introduced at 0-8% (w/w; 0, 1, 2, 3, 4, 5, 6, 7, and 8%). A matched background was prepared by replacing the SL solution with water and adding the same amount of cyclohexanone. Spectra were recorded from 200 to 500 nm.

1.4 Verification of cooperative self-assembly and interactions between SL and EB

A one-factor-at-a-time design was used to evaluate the roles of SL and EB in microsphere formation. When varying SL, EB was fixed at 1 g; when varying EB, SL was fixed at 1 g. The oil phase contained cyclohexanone (10 g), emulsifier 603# (1 g), and EB (1 g by default or varied from 0 to 5 g), while the aqueous phase contained deionized water (40 g) and SL (1 g by default or varied from 0 to 5 g). The aqueous phase was slowly added into the oil phase under stirring (600 rpm) to obtain microsphere dispersions, which were diluted for SEM observation and zeta potential

measurements.

To probe interfacial enrichment and enable semi-quantification of SL/EB in the interfacial emulsion layer, an interfacial settling-separation assay was conducted by dissolving EB (1.5 g) in cyclohexanone (10 g) as the oil phase and dissolving SL (1.5, 2.0, 2.5, or 3.0 g) in water (40 g) as the aqueous phase. The aqueous phase was added first and the oil phase was then introduced slowly along the vessel wall, followed by standing in the dark for 12 h to form an interfacial emulsion layer. The interfacial emulsion (0.1 mL) was diluted with deionized water (19.9 mL) and further diluted 2-, 4-, 6-, 8-, and 10-fold; for each dilution, three parallel aliquots were prepared, filtered through a 0.45 μm organic membrane, and analyzed by excitation-emission matrix (EEM) fluorescence ("3D scan"). EEM spectra were collected using a 1cm × 1 cm four-sided quartz cuvette with excitation scanned from 280 to 470 nm (3 nm step) and emission recorded from 350 to 550 nm, while an additional excitation range of 250-390 nm (2 nm step) was also recorded; both slit widths were 5 nm, response time was set to auto, photomultiplier voltage was 700 V, and scan rate was 12 000 nm min^{-1}. For reference EEM measurements, SL aqueous solutions (0.01-0.05 wt%) were prepared in deionized water, and EB aqueous solutions at the same concentrations were prepared using water pre-adjusted to pH 5; four independent aliquots were collected at each concentration (20 samples per compound), filtered through a 0.45 μm organic membrane, and analyzed under the same EEM conditions.

EB in the interfacial emulsion layer was further compared by HPLC after 12 h standing by diluting the collected interfacial emulsion 10-fold with methanol; EB peak area was used as the quantitative metric for between-treatment comparison. Electrostatic adsorption was additionally examined by adding insoluble SL into an EB-cyclohexanone solution under stirring; after 10 min, the solid was collected by centrifugation, washed three times, dried, and photographed together with pristine SL and EB powders as references.

1.5 Molecular dynamics simulations and computational analysis

Density functional theory (DFT) quantum chemical calculations：Conformational sampling was performed with xtb at the GFN0-xTB level (T = 400 K, 100 ps), saving

snapshots every 50 fs; the resulting structures were ranked to identify the lowest-energy conformer. Quantum chemical calculations were carried out in ORCA 5.0.2 using the B97-3c method, including geometry optimization, frequency analysis, and single-point energy evaluations. Interaction energies were estimated with basis set superposition error (BSSE) correction. Wavefunction files were further analyzed in Multiwfn to obtain molecular electrostatic potential (ESP) maps, AIM topological descriptors, and IGMH analyses, and the results were visualized with VMD 1.9.3.

Molecular dynamics (MD) simulations： All-atom parameters (bonded terms including bonds, angles, and dihedrals) were generated using the force-field utility AuToFF in conjunction with the OPLS-AA force field, and atomic partial charges were assigned using the RESP scheme. [1] Initial configurations were built with Packmol. All simulation boxes were rectangular (8 nm × 8 nm × 14 nm), and cyclohexanone molecules were placed within the top 2 nm region of the box. The numbers of each species were chosen to match the experimental molar ratios.

Two model systems were constructed: System 1, contained 35 lignosulfonate anions and 70 Na^+ counterions (representing SL as dissociated fragments), together with 30 112 H_2O molecules. In addition, 636 cyclohexanone molecules were placed within the top 2 nm region of the simulation box. System 2, contained 35 lignosulfonate anions, 70 Na^+ counterions, and 29 316 H_2O molecules. The top 2 nm region was populated with 636 cyclohexanone molecules, and the system further included 14 emamectin cations and 14 benzoate anions (representing EB as dissociated ionic fragments). All MD simulations were performed using GROMACS 2023.2(GROMACS: High performance molecular simulations through multi-level parallelism from laptops to supercomputers). Energy minimization was carried out with the steepest-descent algorithm for up to 50 000 steps, until the maximum force fell below 100 $kJ \cdot mol^{-1} \cdot nm^{-1}$. Van der Waals interactions were treated with a 1.0 nm cutoff, and long-range electrostatics were computed using the particle-mesh Ewald (PME) method with a real-space cutoff of 1.0 nm.

MD simulation parameters:

Equilibration: The equilibration run was performed using the leap-frog MD

integrator with a 0.0005 ps time step for 100 ps under periodic boundary conditions in all three dimensions. Electrostatics were treated with the particle-mesh Ewald (PME) method using a 1.0 nm real-space cutoff, and van der Waals interactions were truncated at 1.0 nm. Pressure was maintained with a Berendsen barostat (isotropic coupling; time constant 0.5 ps; reference pressure 1 bar; compressibility 4.5×10^{-5} bar^{-1}), while temperature was controlled by a velocity-rescale thermostat (time constant 0.2 ps; reference temperature 298.15 K). All bonds involving hydrogen atoms were constrained.

Production run: The production simulations were carried out using the leap-frog MD integrator with a 0.001 ps time step for 40 ns. Temperature was controlled with a velocity-rescale thermostat (time constant 0.1 ps; reference temperature 298.15 K), and pressure was maintained using a Parrinello-Rahman barostat with isotropic coupling (time constant 2.0 ps; reference pressure 1 bar; compressibility 4.5×10^{-5} bar^{-1}). All other settings were identical to those used in the equilibration stage.

1.6 Encapsulation, release, and loading of EB@MSs/EB@NSs

Encapsulation efficiency determination： Encapsulation efficiency was determined with minor modifications to a previously reported protocol. [2] Briefly, EB@MSs or EB@NSs (0.50 g) was weighed into a clean, dry 100 mL plastic bottle, followed by addition of 10 mL deionized water and 50 mL *n*-hexane. The bottle was placed on a roller mixer and agitated at 60 ± 10 rpm. After mixing, the upper *n*-hexane phase (1 mL) was withdrawn for quantification of free (non-encapsulated) EB (denoted as M_t). In parallel, an aliquot of the same sample was extracted with methanol to determine the total EB content (M_0). EB was quantified by HPLC (Agilent 1200) equipped with a Diamonsil C18 column (250 mm × 4.6 mm, 5 μm), using methanol/water (80:20, v/v) as the mobile phase at 1.0 mL/min and UV detection at 254 nm. All samples were filtered through a 0.22 μm organic membrane prior to injection. Encapsulation efficiency was calculated as:

$$\text{Encapsulation efficiency (\%)} = (M_0 - M_t)/M_0 \times 100\% \quad (1)$$

Where M_0 is the total amount of EB in 0.50 g of the suspension, and M_t is the amount of free (non-encapsulated) EB extracted into the *n*-hexane phase.

Release profile determination： Release behavior was evaluated with slight modifications to the encapsulation-efficiency protocol, using the commercial EC and SC formulations of EB as controls. Briefly, 0.50 g of EB@MSs or EB@NSs was mixed with 1.8 mL deionized water, followed by addition of 112.7 mL *n*-hexane to obtain an initial EB concentration of 100 mg/L in the overall system. The samples were agitated on a roller mixer at 60 ± 10 rpm. At predetermined time points, 1.0 mL of the upper *n*-hexane phase (V_0) was withdrawn and immediately replaced with an equal volume of fresh *n*-hexane. The collected aliquots were filtered through a 0.22 μm organic membrane and analyzed by HPLC to determine the EB concentration in the *n*-hexane phase (C_t). C_t was quantified by HPLC, and the cumulative release proportion was calculated accordingly：

Cumulative release proportion（%）= $[(C_t \times V_0 - M_t)/M_a] \times 100\%$ (2)

Where C_t is the EB concentration in the *n*-hexane phase, V_0 is the sampled *n*-hexane volume, M_t is the amount of free (non-encapsulated) EB, and M_a is the total amount of EB in the system.

Loading content determination： The loading content of EB@MSs and EB@NSs was determined with minor modifications to a literature method.[3] Briefly, 0.50 g of the EB@MSs or EB@NSs formulation was placed in a 50 mL centrifuge tube, mixed with 30 mL deionized water, shaken for 15 s, and centrifuged for 5 min (MSs: 2000 rpm; NSs: 4000 rpm). The precipitate was collected and dried at 50 °C to obtain solid microspheres (MS) or nanospheres (NS). A known mass (M_1, mg) of the dried MS/NS solids was then dispersed in methanol (V_1, mL) in a 50 mL tube, ultrasonicated for 30 min, and further extracted by shaking for 5 min. An aliquot of the supernatant (1 mL) was diluted N_0-fold with methanol/water (80:20, v/v), filtered through a 0.22 μm organic membrane, and analyzed by HPLC to determine the EB concentration (C_t, mg/L).

The loading content of EB in MSs and NSs was calculated using the following equation:

Loading content (%) = $(C_t \times V_1 \times N_0)/M_1 \times 100\%$ (3)

Where C_t is the EB concentration, V_1 is the methanol volume, N_0 is the dilution factor, and M_1 is the mass of the dried MS/NS solids.

1.7 Foliar UV photostability of EB@MSs and EB@NSs on cabbage leaves

Foliar photostability was compared among formulations using EB-EC, EB-SC, and SC@SL as references. Cabbage leaves were cut into 3 cm × 6 cm rectangles, and each piece was uniformly coated with 0.2 mL of a 1000 mg/L working suspension/solution of EB-EC, EB-SC, SC@SL, EB@MSs, or EB@NSs. The treated leaves were air-dried in the dark for 4 h and then irradiated in a UV aging chamber at 30 °C with a UV intensity of 35 $\mu W \cdot cm^{-2}$. Samples were collected at 0, 15, 30, 60, 90, 120, 180, and 240 min. The EB residue on leaves at each time point was quantified by HPLC as described above, and the residue percentage was calculated as follows:

$$\text{Residue of EB}\ (\%) = (C_t \times V_1)/M_a \times 100\% \qquad (4)$$

Where C_t is the EB concentration, V_1 is the methanol volume, and M_a is the total amount of EB applied.

1.8 Multi-target pest bioassays

Leaf-dip bioassay for Agrotis segetum: Four EB formulations (SC, EC, NSs, and MSs) were serially diluted with deionized water to obtain a range of test concentrations. Cabbage leaf discs (1 cm diameter) were immersed in each working solution for 20 s, removed, and air-dried under ambient conditions. Two treated discs were placed in each well of a 24-well plate, and one third-instar *Agrotis ipsilon* larva was introduced per well (24 larvae per treatment). Bioassays were conducted at 25 ± 1 °C and 70 ± 5% relative humidity. Mortality was recorded at 24 and 72 h post-treatment. Deionized water served as the control, and each concentration was tested in triplicate.

Greenhouse pot assay against Frankliniella occidentalis: Cucumber plants with naturally established thrips infestations were selected in a greenhouse. The four EB formulations were diluted with deionized water to provide active-ingredient concentrations of 10, 5, and 2.5 mg/L, and 0.01% (v/v) organosilicone adjuvant was added. Using a hand-held sprayer, 30 mL of working solution was applied uniformly to both the adaxial and abaxial leaf surfaces. For each treatment, three leaves on the same plant were used as replicates. The control received deionized water containing 0.01%

organosilicone adjuvant. Thrips populations were counted before treatment and at 1, 3, 5, and 7 d post-treatment. Population reduction was calculated as:

Population reduction (%) = $(N_0 – N_t)/N_0 \times 100\%$

Where N_0 is the pre-treatment thrips count and N_t is the count at each sampling time point.

Field efficacy trial against Spodoptera exigua on cabbage: A field trial was conducted in a cabbage-growing area at Sankeshu Family Farm, Fangcun Town, Daiyue District, Tai'an, Shandong, China (35.96519°N, 117.17581°E). Uniform cabbage plants 2 weeks after transplanting were selected. Each plot measured 15 m² and contained ≥40 plants, with 1.0 m buffer zones between plots. Baseline larval density was recorded before application, and the application rate was calculated based on the recommended dose registered on the China Pesticide Information Network (3.4 g a.i./ha). The four EB formulations were prepared as 25 mg/L working suspensions and supplemented with 0.01% (v/v) organosilicone wetting agent; the control was deionized water containing 0.01% organosilicone. Treatments were arranged with three replicates, and 2 L of spray solution per plot was applied until leaves were uniformly wetted. Larval counts were assessed at 1, 7, and 14 d after treatment, and population reduction was calculated accordingly.

1.9 UV pre-irradiation bioassays

UV-Preirradiation Bioassay (Leaf-Dip Method): Four EB formulations (SC, EC, NSs, and MSs) were prepared at 25 and 50 mg/L (a.i.) using deionized water. Cabbage leaf discs (1 cm diameter) were dipped for 20 s, air-dried, and preirradiated in a UV-aging chamber (40 μW·cm^{-2}, 30 °C) for 0, 30, 60, 120, 180, or 240 min. After irradiation, two discs were placed in each well of a 24-well plate and one third-instar *Agrotis ipsilon* larva was introduced per well (24 larvae per treatment). Bioassays were conducted at 25 ± 1 °C and 70 ± 5% relative humidity, with mortality recorded at 24 and 72 h. Deionized water served as the control, and each treatment was tested in triplicate.

UV-Exposure Feeding Phenotype Assay (leaf damage assessment): The four EB formulations (SC, EC, NSs, and MSs) were prepared at 50 mg/L (a.i.) with deionized

water. Cabbage leaf discs (6 cm diameter) were dipped for 20 s, air-dried, and then irradiated in a UV-aging chamber (40 μW·cm^{-2}, 30 °C) for 0 or 120 min. Each irradiated disc was fixed to the bottom of a Petri dish using double-sided tape, and 12 third-instar *Agrotis ipsilon* larvae were introduced per dish. Assays were conducted under the same environmental conditions described above (25 ± 1 °C, 70 ± 5% RH). Mortality was recorded at 24 h, and feeding damage was documented photographically. Deionized water served as the control, and each treatment was performed in triplicate.

1.10 Non-target Ecological Safety

Acute immobilization test with Daphnia magna: Acute immobilization of *Daphnia magna* was evaluated for the four EB formulations (SC, EC, NSs, and MSs). Test solutions were prepared in aerated, dechlorinated tap water at nominal EB concentrations of 0.001, 0.01, 0.1, 1, 10, and 100 mg/L, with aerated water serving as the blank control. Assays were conducted in an incubator at 20 ± 2 °C. For each concentration, 40 mL of test solution was added to a 50 mL beaker and 15 *D. magna* individuals were introduced; three replicates were set for each treatment and the control. Immobilized individuals were counted at 24 and 48 h. An organism was scored as immobilized if it was unable to swim within 15 s after gentle agitation of the beaker.

Leaf-disc assay for Amblyseius cucumeris (non-target safety): A leaf-disc bioassay was conducted following the referenced method cited in the main text. Working suspensions of the four EB formulations (SC, EC, NSs, and MSs) were prepared in water at 6.25, 12.5, 25, 50, 100, and 200 mg/L. Each concentration was tested in triplicate, with water as the blank control. Cucumber leaves were punched into 4-cm-diameter discs and individually dipped into the test suspensions for 5-10 s, then air-dried. The discs were placed abaxial side up on moist sponge positioned in the center of a 6 cm (diameter) × 1.5 cm (height) Petri dish; deionized water was added to approximately one-third of the sponge height to maintain humidity. Adult *A. cucumeris* were gently transferred onto the abaxial surface using a fine brush (20 mites per disc). Assays were maintained in a climate chamber at 25 ± 1 °C, 75 ± 5% relative humidity, and a 16:8 h (L:D) photoperiod. Mortality was assessed at 24 and 48 h under a

stereomicroscope; individuals showing no response to gentle probing with a brush were recorded as dead, and mortality was calculated accordingly.

1.11 Functional validation of the one-step strategy using abamectin

1.11.1 Preparation of ABM@NSs and ABM@MSs

ABM@MSs and ABM@NSs were prepared using the same one-step self-assembly strategy described for EB@MSs and EB@NSs in the main text, with minor optimization of the formulation composition and operating parameters for abamectin. In accordance with pesticide registration requirements, abamectin formulations with an active ingredient content of 3% were prepared. The optimized formulations selected for validation, based on particle morphology, dispersion stability, and size distribution, exhibited D50 values of 2.82 μm for ABM@MSs and 276 nm for ABM@NSs.

1.11.2 Release profile determination of abamectin

The release behavior of abamectin was determined using the same procedure as that described above for EB, with slight modifications, using the conventional suspension concentrate (SC) and emulsifiable concentrate (EC) formulations of abamectin as controls. Briefly, the abamectin micro-/nanosphere suspension was diluted with deionized water to an abamectin concentration of 200 mg/L, and 10 mL of the diluted suspension was introduced into a glass bottle containing 50 mL n-hexane and 40 mL deionized water. The mixture was agitated on a roller mixer at 70 ± 10 rpm. At predetermined time intervals, 1.0 mL of the upper n-hexane phase was withdrawn, immediately replaced with an equal volume of fresh n-hexane, filtered through a 0.22 μm organic membrane, and analyzed by HPLC using an Agilent 1200 system fitted with an Agilent Diamonsil C18 column (250 mm × 4.6 mm, 5 μm). The mobile phase was acetonitrile/water (85:15, v/v) at a flow rate of 1.0 mL/min, and detection was performed at 254 nm. The cumulative release proportion was calculated according to Eq. (2).

1.11.3 Toxicity of abamectin formulations against *Meloidogyne incognita* J2

A population of Meloidogyne incognita was collected from tomato roots showing severe root-knot symptoms in a solar greenhouse in Dongdawu Village, Dawenkou Town, Daiyue District, Tai'an, Shandong Province, China. The species was identified

by morphological and molecular analyses and subsequently maintained on greenhouse-grown cucumber plants. Dispersed eggs were placed on a 500-mesh hatching sieve and incubated in the dark at 25 °C. Newly hatched second-stage juveniles (J2) were collected daily for the bioassays.

The toxicity of four abamectin formulations, namely SC, EC, NSs and MSs, against M. incognita J2 was evaluated using a nematode immersion assay. Each formulation was diluted with 0.1% Tween-80 aqueous solution to prepare a 10000 mg/L stock solution, which was then serially diluted to active ingredient concentrations of 0.125, 0.25, 0.5, 1 and 2 mg/L.

Bioassays were conducted in 24-well cell culture plates. Briefly, 0.30 mL of treatment solution and 0.30 mL of a concentrated J2 suspension were added to each well and mixed gently. The nematode suspension contained approximately 400 juveniles per mL. Plates were incubated in the dark at 25 ± 2 °C, with 0.1% Tween-80 aqueous solution as the control. The numbers of dead nematodes and total nematodes were recorded under a stereomicroscope after 24 and 48 h of exposure. Nematodes were considered dead when they remained rigid and immobile after gentle probing with a fine needle. Each concentration was tested in triplicate, and the experiment was independently repeated three times. Mortality was calculated as follows:

Mortality (%) = (number of dead nematodes/total number of nematodes) × 100% (5)

1.11.4 Soil leaching behaviour of abamectin formulations

Soil leaching experiments were carried out in PVC columns (5 × 5 × 15 cm) using four abamectin formulations (SC, EC, NSs, and MSs). Soil was collected from an experimental farm in Tai'an, Shandong, China (117.11°E, 36.19°N), and classified as silty loam. Surface soil (0-30 cm) was air-dried, homogenized, and passed through a 20-mesh sieve prior to use. For each treatment, soil was packed into the PVC column to a height of 12 cm. To simulate field application, each formulation was diluted with 0.1% Tween-80 aqueous solution to give an equivalent active ingredient concentration of 20 mg/L, and 100 mL of the resulting dispersion was applied to each column until the soil reached saturation. After complete infiltration, the column was sectioned into twelve 1 cm layers to determine the vertical distribution of abamectin in the soil profile.

The soil samples were then dried, extracted with acetonitrile, and analysed by HPLC (Agilent 1200, Agilent Technologies, Santa Clara, CA, USA) using an Agilent Diamonsil C18 column (250 mm × 4.6 mm i.d., 5 μm) with acetonitrile/water (85:15, v/v) as the mobile phase at 1.0 mL/min and detection at 254 nm. All experiments were performed in triplicate.

2. Supporting Figures

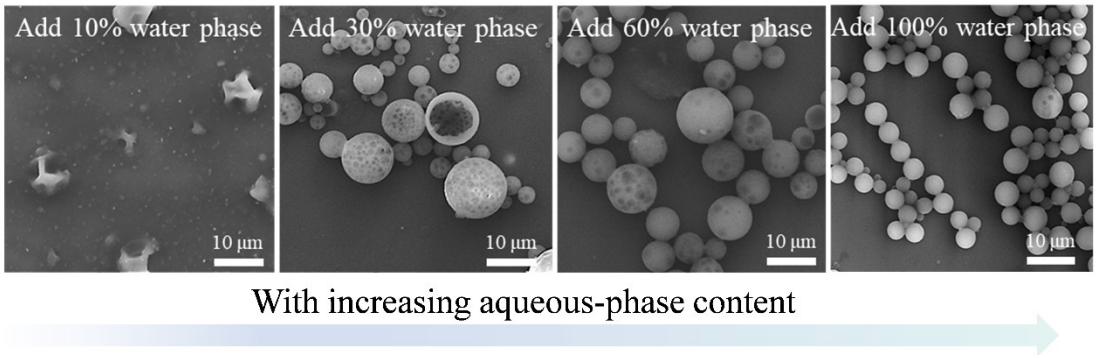

Figure S1. SEM micrographs illustrating microsphere formation at different aqueous-phase addition levels (10-100%).

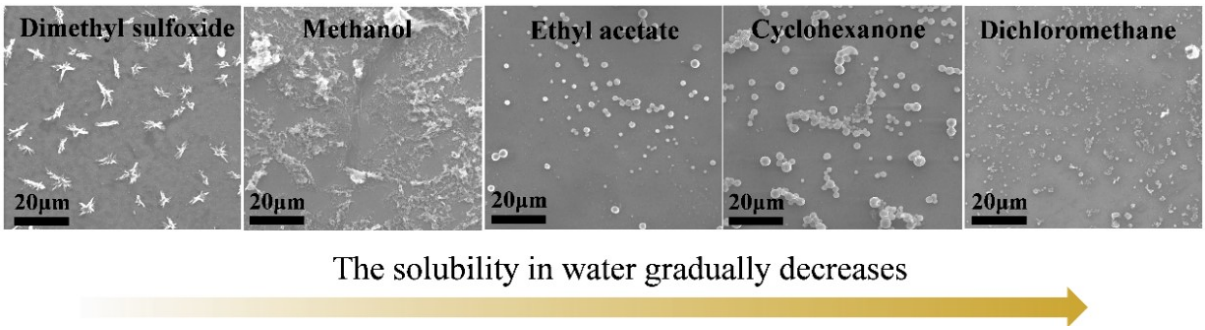

Figure S2. SEM images of microspheres prepared under different solvent-induction.

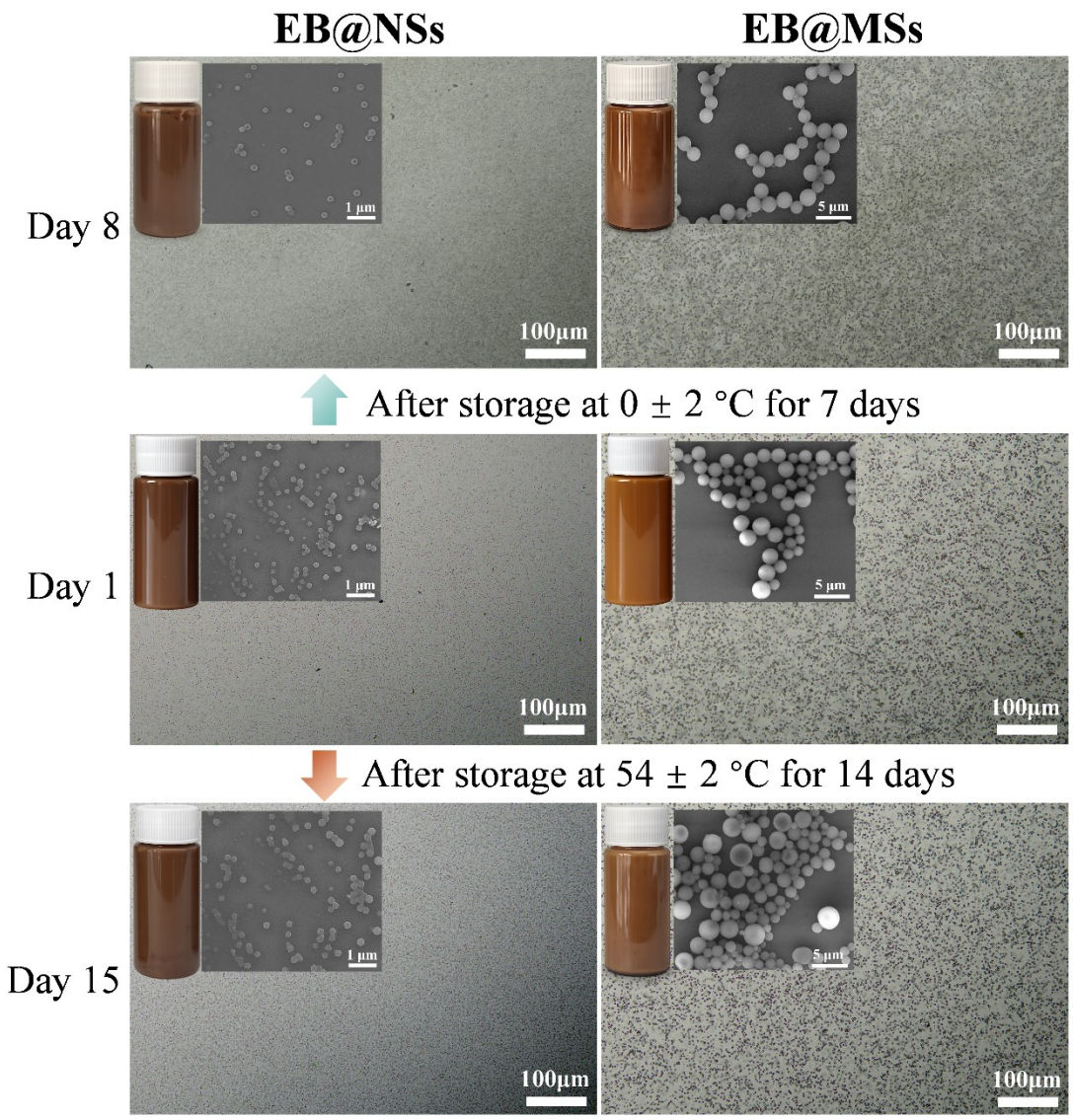

Figure S3. Accelerated storage stability test of EB@MSs and EB@NSs. Accelerated storage stability of EB@MSs and EB@NSs. After storage at 0 ± 2°C for 7 d and 54 ± 2°C for 14 d, no obvious changes were observed in physical appearance, particle size, dispersion state, or particle morphology.

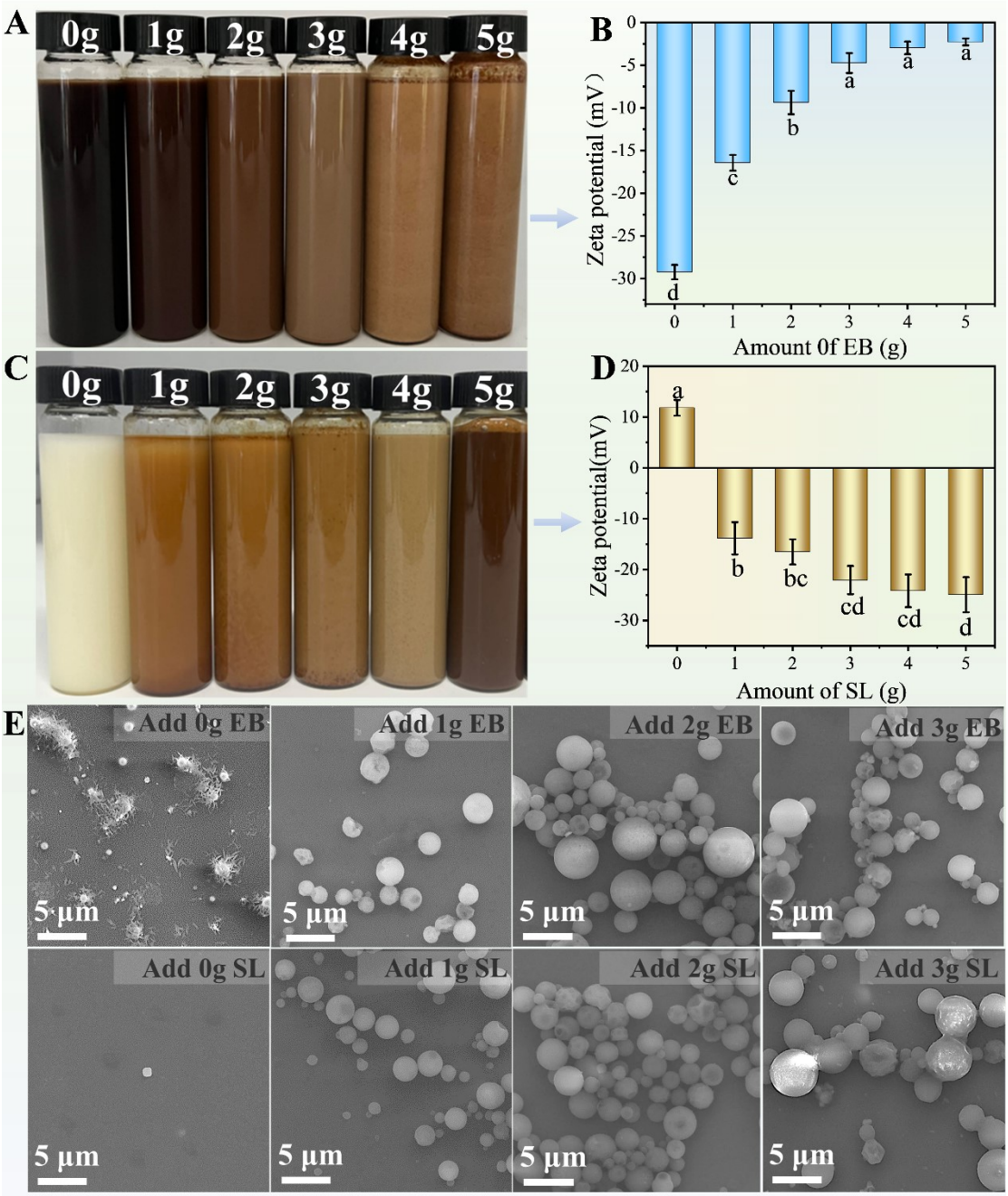

Figure S4. Single-factor and ratio regulation of EB/SL on microsphere formation, confirming that both EB and SL are essential components. (A) Visual appearance of the formulations at varying EB dosages. (B) zeta potential of the system as a function of EB dosage. (C) Visual appearance of the formulations at varying SL dosages. (D) zeta potential of the system as a function of SL dosage. (E) SEM morphologies of particles prepared with different EB or SL dosages. Data were displayed as mean ± SE and the difference analysis was conducted by Tukey's test at the $p < 0.05$ level.

Single-factor regulation shows that the dosages and ratio of EB and SL jointly govern the formulation appearance, zeta potential, and particle morphology. Upon introducing SL, the zeta potential shifts from positive to negative and gradually levels off with increasing SL content, indicating that EB-SL association is dominated by electrostatic complexation with a saturation tendency. SEM observations further reveal a morphological evolution from disordered aggregates/trace crystals to thin-shelled microspheres, followed by shell thickening and structural densification. Overall, both EB and SL are indispensable for microsphere formation, and their interactions and compositional window determine the robustness of microsphere generation and the final architecture (Figure S4)

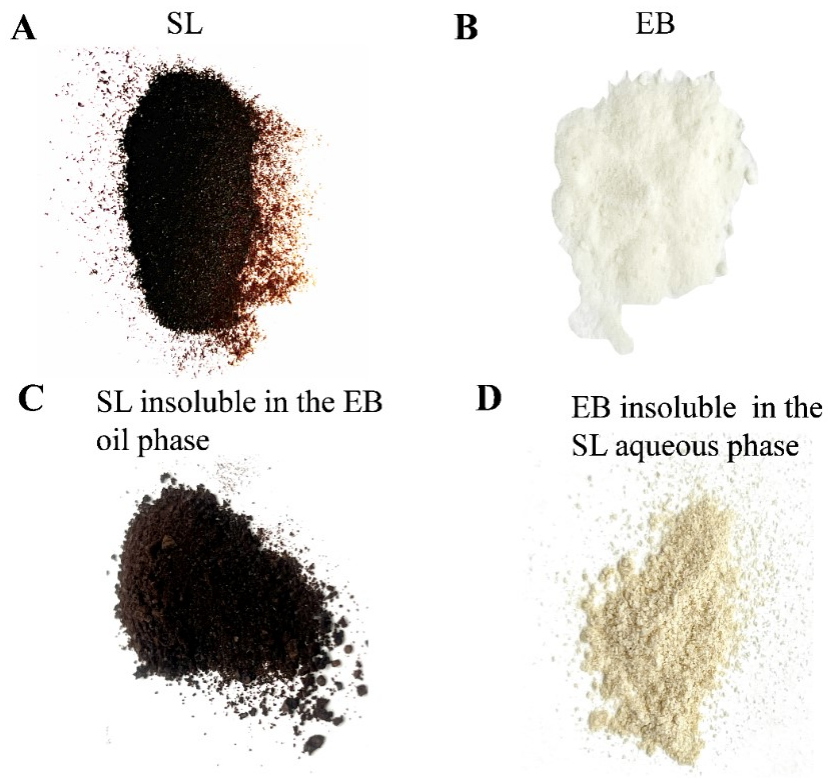

Figure S5. Solid-state appearance of EB and SL and verification of their mutual adsorption. (A) Pristine SL. (B) Pristine EB. (C) Solid collected after adding SL to an EB/cyclohexanone solution, followed by three cycles of centrifugation, washing, and drying. (D) Solid collected after adding EB to an aqueous SL solution, followed by three cycles of centrifugation, washing, and drying.

As shown by the neat material, SL appears as dark brown/black fine particles, whereas EB is an off-white powder. After contacting SL with an EB/cyclohexanone solution, the recovered SL (Figure S4C) remained dark, making the adsorption of trace EB difficult to discern visually. In contrast, EB recovered after contacting an aqueous SL solution (Figure S4D) turned from off-white to distinctly darker, suggesting that EB can adsorb and co-carry dissolved SL components from solution. Collectively, these observations support a mutual adsorption interaction between EB and SL (Figure S5).

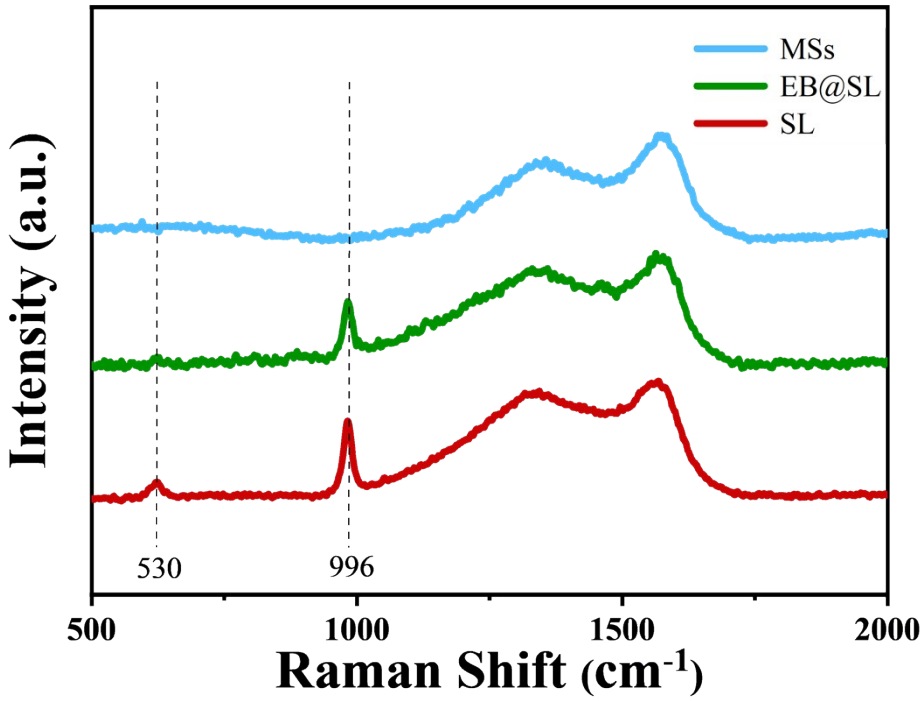

Figure S6. Raman spectrum of SL、EB@SL and MSs.

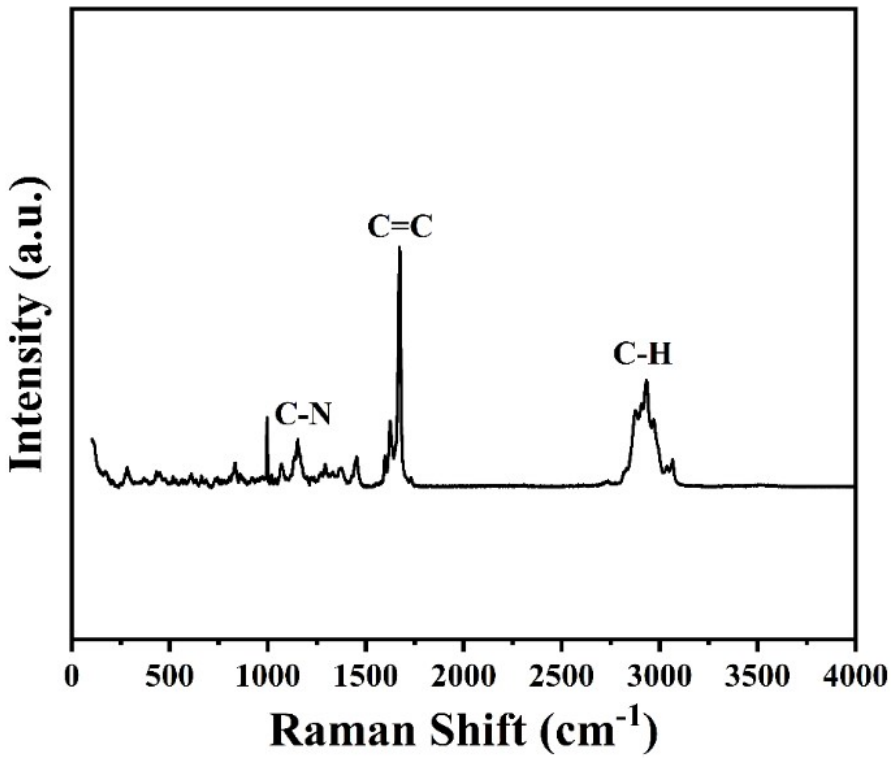

Figure S7. Raman spectrum of EB.

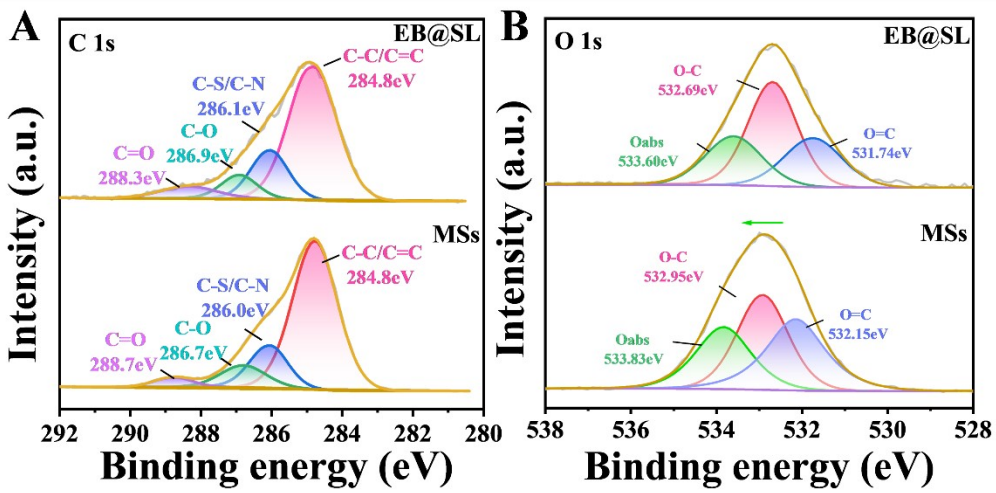

Figure S8. (A) High-resolution C 1s XPS spectrum with peak deconvolution; (B) high-resolution O 1s XPS spectrum with peak deconvolution (top: EB@SL; bottom: MSs).

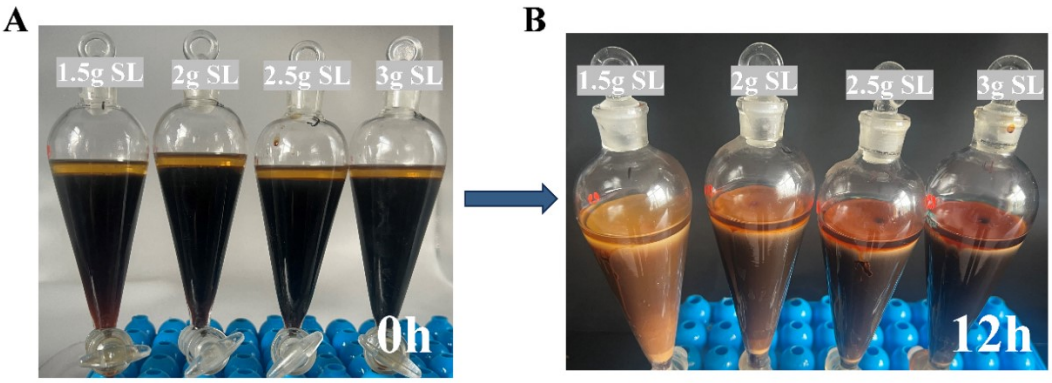

F**igure S9.** Emulsion-layer separation setup and interfacial phase formation. (A) Immediately after combining the two phases (0 h): the upper phase is EB dissolved in cyclohexanone, and the lower phase is an aqueous SL solution with varying SL masses. (B) Top view after 12 h of standing: a distinct interfacial emulsion layer forms between the oil and water phases (collected for subsequent quantitative/semi-quantitative analyses); the oil phase becomes progressively darker as the SL content in the aqueous phase increases. Given that SL is insoluble in cyclohexanone, this trend suggests that EB promotes SL enrichment toward the interface/oil phase.

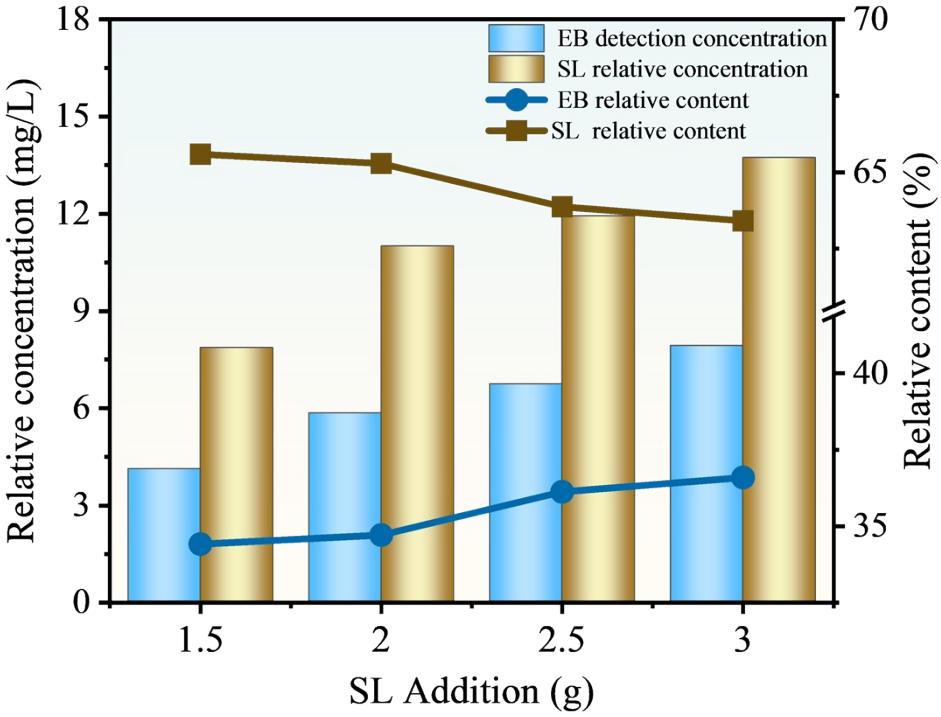

Figure S10. The absolute EB concentration measured by HPLC was used as the calibration reference, and the EEM-PARAFAC *F*max values (reflecting the relative contribution of each component) were combined to derive the relative fraction of EB. The corresponding *F*max for the SL component was then used to estimate its relative abundance, which was further converted to the relative concentration of SL.

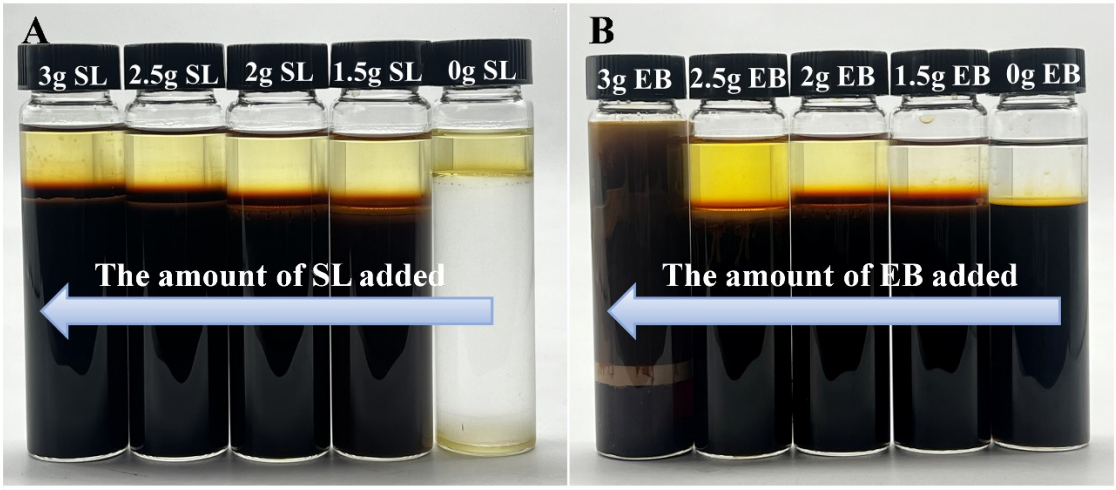

Figure S11. Single-factor regulation indicates that EB and SL promote interfacial enrichment and the formation of a stable emulsion layer. Photographs were taken after standing for 12 h following addition of the oil phase (upper layer) and aqueous phase (lower layer): (A) varying the SL dosage in the aqueous phase while keeping the oil phase constant; (B) varying the EB dosage in the oil phase while keeping the aqueous phase constant.

Single-factor tests show that aqueous SL and oil-phase EB undergo interfacial enrichment and mutual attraction during standing. In the absence of SL, partial dissolution of cyclohexanone into the water phase leads to turbidity; upon adding SL, a stable interface is established, and increasing either SL or EB progressively deepens the color of the oil near the interface and extends this darkened region upward. Because SL is insoluble in cyclohexanone, these observations indicate that EB promotes SL enrichment toward the interface/oil phase and facilitates complex formation. Although phase inversion occurs at high EB loading, it does not alter the overall trend (Figure S11)

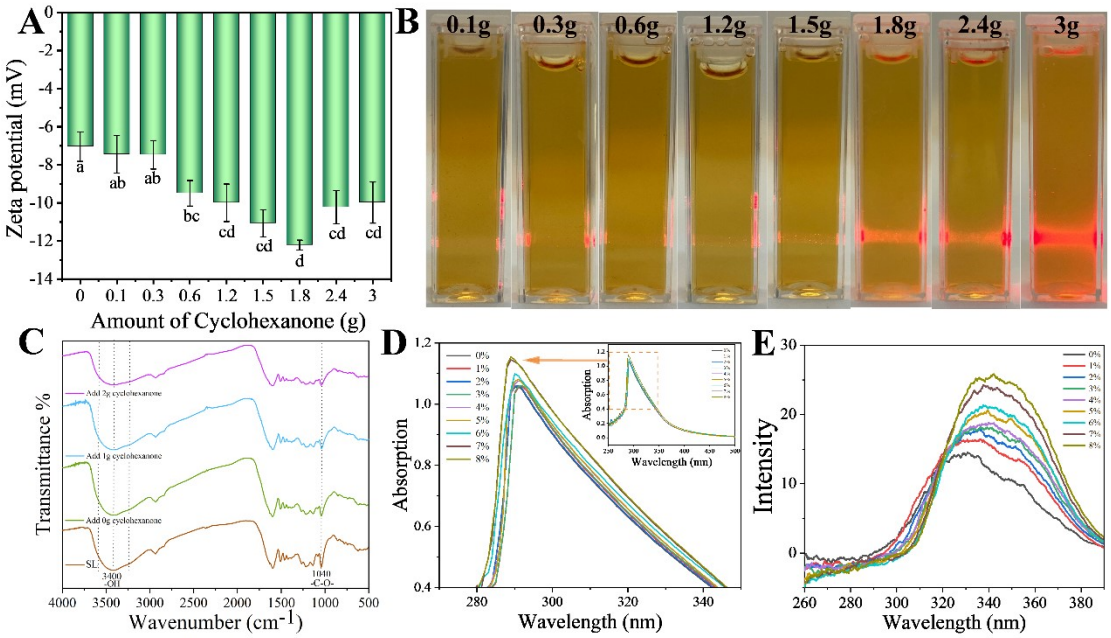

Figure S12. Cyclohexanone dosage induces aggregation/conformational rearrangement in the SL system, accompanied by coupled changes in zeta potential and multimodal spectroscopic signatures. (A) zeta potential of the SL dispersion at different cyclohexanone dosages. (B) Tyndall effect observed at different cyclohexanone dosages. (C) FTIR spectra of solids collected by centrifugation from the mixtures. (D) UV-vis absorption spectra of the mixtures. (E) Fluorescence excitation spectra of the mixtures. Data were displayed as mean ± SE and the difference analysis was conducted by Tukey's test at the $p < 0.05$ level.

The solvent-displacement process involving cyclohexanone markedly regulates the colloidal stability and molecular conformation of SL in the aqueous phase, thereby triggering self-assembly and aggregation. As the cyclohexanone dosage increases, the Zeta-potential exhibits a pronounced non-monotonic variation and reaches a regime with the strongest Tyndall scattering, indicating a transition of SL from a relatively dispersed state to higher-order aggregates; excessive cyclohexanone, however, weakens these aggregates and drives the system parameters toward a steady state. In parallel, the UV-vis absorbance increases with cyclohexanone fraction, while characteristic FTIR bands of the centrifuged solids broadly attenuate, suggesting changes in the microenvironment of aromatic backbone-related moieties, potentially

associated with molecular folding and/or enhanced spatial conjugation. The fluorescence excitation spectra intensify overall without appreciable changes in spectral profile or peak position, implying that aggregation primarily enhances the effective absorption of emissive centers and improves emission efficiency (quantum yield), consistent with aggregation-induced emission (AIE) where restricted intramolecular motions increase the radiative transition contribution.[4–6] Collectively, these results show that cyclohexanone dosage dictates the aggregation level and conformational state of SL, providing an experimental basis for selecting the solvent window used for subsequent microsphere formation (Figure S12).

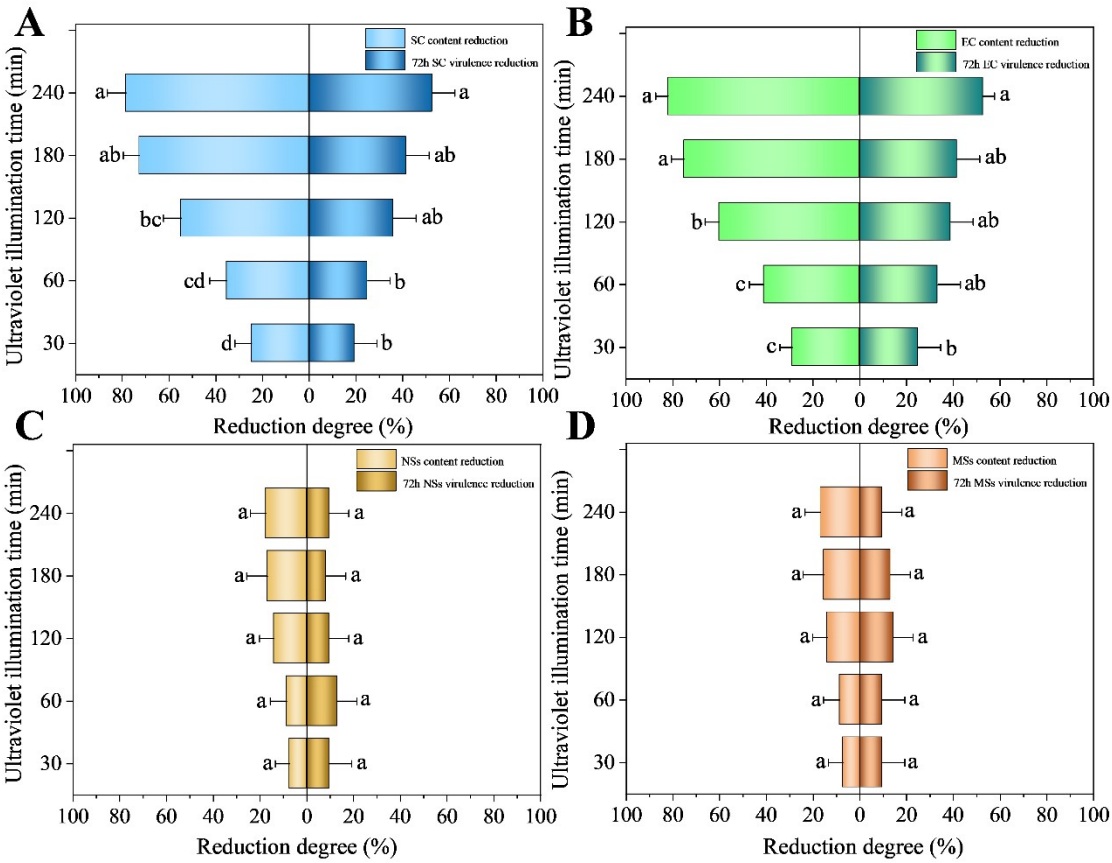

Figure S13. Using the pre-photolysis active-ingredient content and bioassay mortality as baselines, the correspondence between "active-ingredient loss" and the reduction in 72 h mortality of *Agrotis ipsilon* after photolysis was compared across formulations. (A) SC; (B) EC; (C) NSs; (D) MSs. In each panel, the left axis denotes the amount of active ingredient degraded, and the right axis denotes the corresponding decrease in 72 h mortality of *A. segetum*. Data are presented as mean ± SD. Different letters indicate significant differences (Tukey's test, $p < 0.05$); values sharing the same letter are not significantly different.

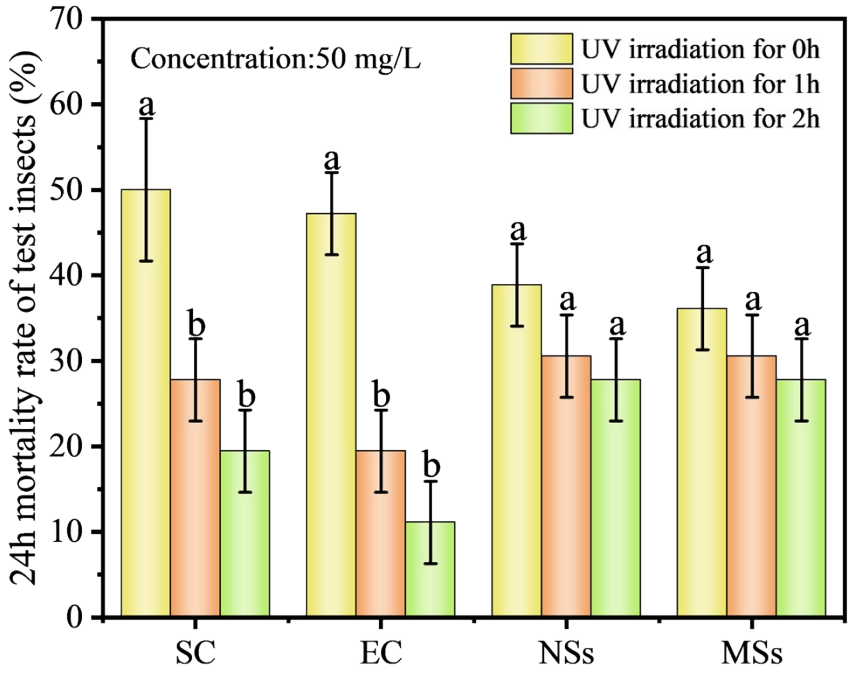

Figure S14. Effect of UV irradiation duration on the foliar toxicity of different EB formulations. Leaves were immersed in diluted EB formulations (SC, EC, NSs, and MSs), exposed to UV irradiation for 0, 1, or 2 h, and then fixed in Petri dishes for insect exposure. Mortality was recorded 24 h after treatment. Data are presented as mean ± SD. Different letters indicate significant differences (Tukey's test, $p < 0.05$); values sharing the same letter are not significantly different.

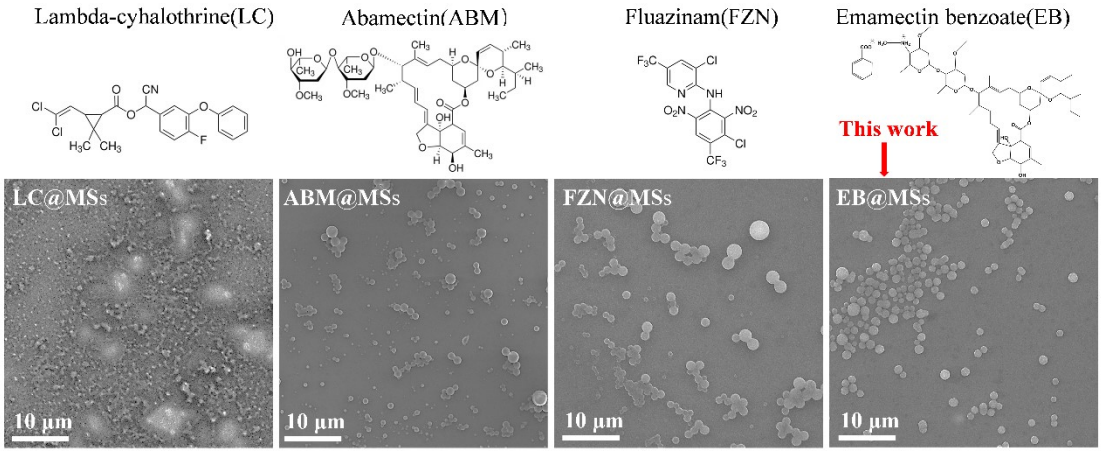

Figure S15. Generality verification of the one-pot process for lignin-based pesticide delivery systems: under identical processing parameters, different technical-grade active ingredients were introduced into the formulation, and the resulting particles were characterized by SEM to compare their morphologies.

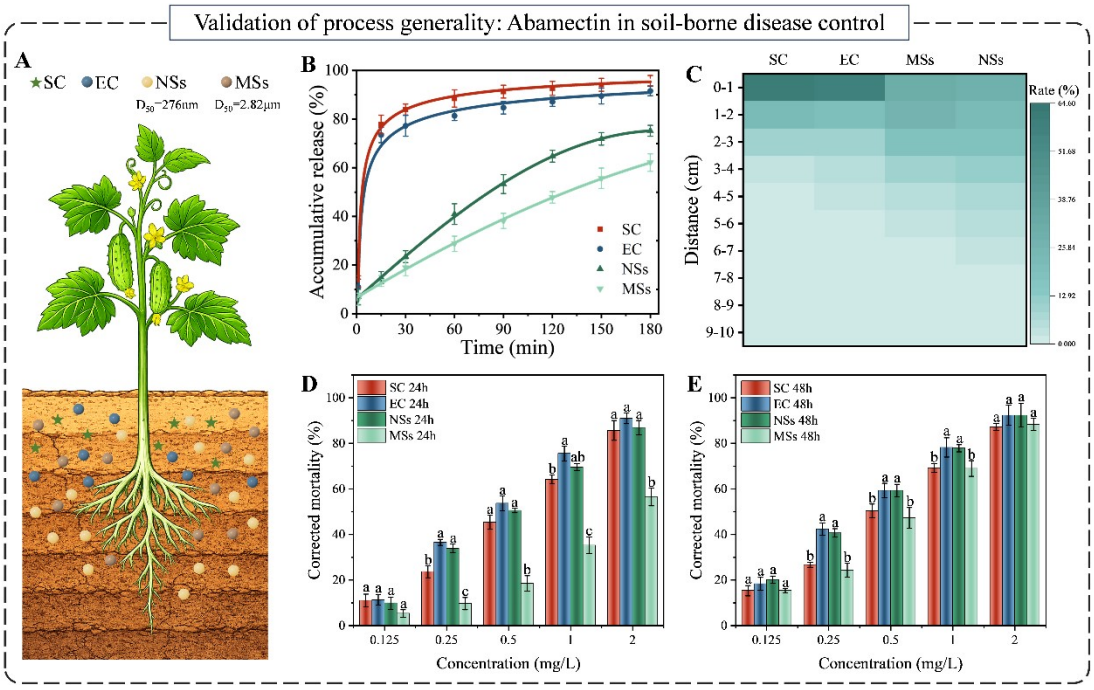

Figure S16. Validation of process generality using abamectin for soil-borne disease control. (A) Schematic diagram of the soil leaching experiment. (B) Fitted release kinetics of the four formulations. (C) Migration of abamectin in soil for different formulations. Nematicidal activities of ABM@NSs (D50=276nm) and ABM@MSs (D50=2.82μm) at (D) 24 h and (E) 48 h. The abamectin formulations were ABM SC (suspension concentrate), ABM EC (emulsifiable concentrate), ABM@NSs, and ABM@MSs. Data are mean ± SD; different lowercase letters indicate significant differences (Tukey's test, $n = 3$, $p < 0.05$).

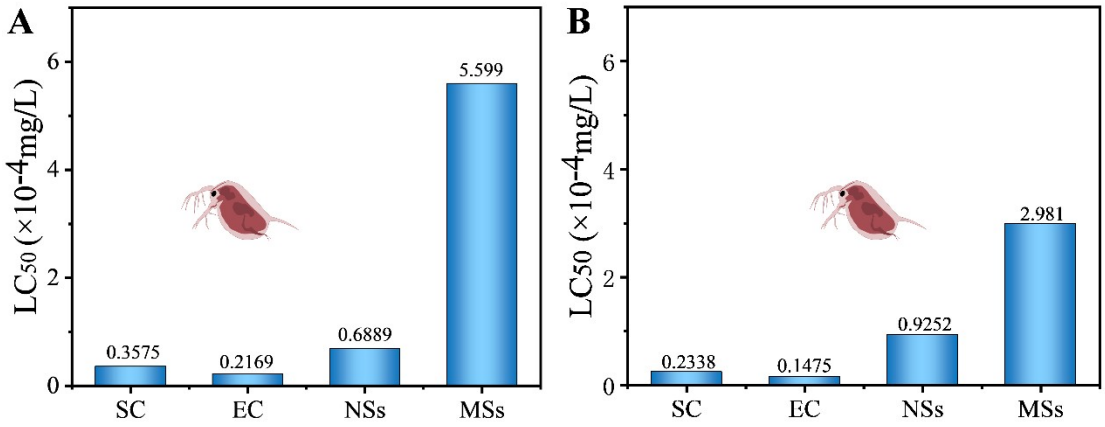

Figure S17. (A, B) Acute toxicity of four EB formulations (SC, EC, MSs, and NSs) to *Daphnia magna*, expressed as LC_{50} values at 24 h and 48 h.

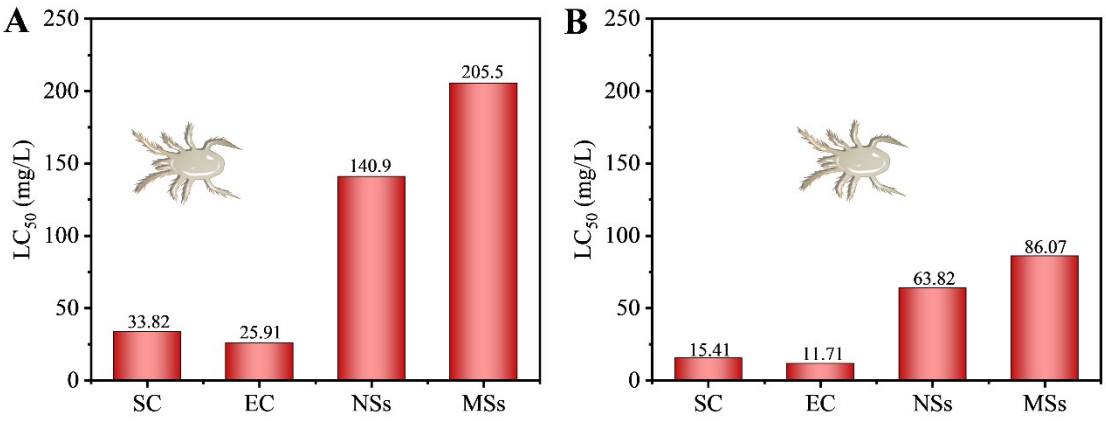

Figure S18. (A, B) Acute toxicity of four EB formulations (SC, EC, MSs, and NSs) to *Amblyseius cucumeris*, expressed as LC_{50} values at 24 h and 48 h.

3. Supporting Tables

Table S1. The loading efficiency and encapsulation efficiency of samples.

Sample	Loading efficiency (%)	Encapsulation efficiency (%)
EB@MSs	31.54 ± 1.35% a	92.04 ± 1.24% a
EB@NSs	25.31 ± 1.17% b	89.95 ± 1.63% a

Data are displayed as mean ± SE, and the difference analysis between treatments in terms of the drug loading rate at the same time was done by Tukey's test at the $p < 0.05$ level.

Table S2. Hydrogen bond characteristics at BCP of complexes.

BCP	ρ(r)(a.u.)	$\nabla^2\rho$(r)(a.u.)	V(r)(a.u.)	H(r)(a.u.)
1	0.0559	0.1507	-0.0590	-0.0106
2	0.0461	0.1337	-0.0461	-0.0063
3	0.0482	0.1331	-0.0494	-0.0080

Table S3. Accelerated storage stability of EB@MSs and EB@NSs at 2.3%.

Testing items	pH value	Particle size (μm)	Total content of a.i./%	Zeta potential (mV)
EB@MSs	7.3 ± 0.1	2.54 ± 0.25	2.28 ± 0.01	-35.43 ± 1.25
Cold storage	7.0 ± 0.2	2.38 ± 0.33	2.26 ± 0.01	-33.26 ± 2.11
Thermal storage	7.1 ± 0.2	2.89 ± 0.41	2.21 ± 0.02	-32.78 ± 2.25
EB@NSs	7.4 ± 0.1	0.283 ± 0.01	2.28 ± 0.01	-37.74 ± 1.84
Cold storage	7.2 ± 0.1	0.245 ± 0.02	2.24 ± 0.02	-36.42 ± 2.65
Thermal storage	7.3 ± 0.2	0.295 ± 0.02	2.23 ± 0.02	-34.58 ± 3.11

Table S4: Production time and energy consumption calculation for four dosage forms.

Category and Power	Processing time of SC	Processing time of EC	Processing time of NSs	Processing time of MSs
Material preparation and addition stage	—	—	—	—
Mixing and stirring power：10 kW/(t·h)	0.2h	1h	1h	1h
Pre-mixing and cutting power：30 kW/(t·h)	0.3h	0h	0h	0h
First-stage bead mill power: 40 kW/(t·h)	2.5h in series	0h	0h	0h
Second-stage bead mill power: 45 kW/(t·h)		0h	0h	0h
Third-stage bead mill power: 50 kW/(t·h)		0h	0h	0h
Post-mixing poweR：50 kW/(t·h)	0.5h	0h	0h	0h
Total processing time	**3.5h**	**1h**	**1h**	**1h**
Cooling-water system power: 8 kW/(t·h)	2.5h	0h	0h	0h
Total energy consumption (kWh)	**393.5**	**10**	**10**	**10**
References	[7]	[8]	[9]	

All formulations followed standard lab procedures with minor industrially aligned workflow/time adjustments; power inputs matched the company's scale-up specs. Note: kW/(t·h) is power per unit throughput; three-stage bead mills run simultaneously.

Table S5. Direct production costs of four formulations (raw materials and energy).

Category	Unit price (RMB/ton)	Quantity of Process SC	Quantity of Process EC	Quantity of Process NSs	Quantity of Process MSs
Emamectin Benzoate	Excluded	2.3%	2.3%	2.3%	2.3%
Sodium Lignosulfonate	8500	0%	0%	4%	3%
Xanthan gum	23000	0.15%	0%	0%	0.1%
Magnesium Aluminum Silicate	11000	1%	0%	0%	0.5%
Cyclohexanone	16000	0%	10%	8%	10%
Butylated Hydroxy Toluene	20000	1%	1%	0%	0%
Xylene	7500	0%	76.7%	0%	0%
Emulsifier 603#	25000	3%	5%	4%	3%
Emulsifier 500#	19000	2%	5%	0%	0%
Ethylene Glycol	7500	2%	0%	0%	0%
Ingredient water	5	88.55%	0%	81.7%	81.1%
Cooling water	5	2t	0t	0t	0t
Raw Material Cost (CNY/ton)	Without EB	1638.9	9752.5	2624.1	2687.1
Industrial electricity cost（CNY/kWh）	0.8	314.8	8	8	8
Direct production cost (CNY/ton)	—	1953.7	9760.5	2632.1	2695.1
Direct production cost (USD/ton)	1USD ≈7.1235CNY	**274.2**	**1370.1**	**369.4**	**378.3**
References	—	[10]	[11]	[12]	
Price Reference Website	https://m.chinabgao.com				
Formulation proportions	Cost estimates are based on parameters obtained through technical exchanges with industry; the data were anonymized and reconciled for consistency.				

Table S6. Evaluation methods for non-target safety and efficacy against target pests.

Evaluation	Evaluation approach
Control efficacy	Control efficacy was derived from bioassays at the highest tested concentration for each formulation against *Agrotis segetum*, *Frankliniella occidentalis*, and *Spodoptera exigua*. For each pest, a composite endpoint (day 1 + final-day mortality or population reduction) was calculated to capture rapid and residual effects, normalized, and then averaged across pests to obtain an overall efficacy score.
Safety assessment	Safety was evaluated using the 24 h and 48 h acute toxicity LC_{50} values of the four formulations for two non-target organisms (*Daphnia magna* and *Amblyseius cucumeris*). For each organism, LC_{50}-based metrics were normalized, and the normalized scores were then averaged across organisms to yield an overall safety score.

Table S7. Normalized scores for various aspects of EB in four formulations.

Category	Normalized score of SC	Normalized score of EC	Normalized score of NSs	Normalized score of MSs
Direct production cost advantage	100	20	74.2	72.5
Processing time advantage	28.6	100	100	100
Energy consumption advantage	1.6	100	100	100
Control efficacy	87.66	87.54	100	89.07
Environmental safety	11.89	8.57	50.8	100

References

1. B. Doherty, X. Zhong, S. Gathiaka, B. Li and O. Acevedo, *J. Chem. Theory Comput.*, 2017, **13**, 6131–6145.

2. H. Cao, Y. Chen, D. Zhang, Y. Jin, P. Zhang, B. Li, W. Mu, F. Liu and H. Cao, *Chem. Eng. J.*, 2022, **439**, 135805.

3. Y. Shen, H. Zhu, J. Cui, A. Wang, X. Zhao, B. Cui, Y. Wang and H. Cui, *Nanomaterials*, 2018, **8**, 1016.

4. A. V. Fonin, A. I. Sulatskaya, I. M. Kuznetsova and K. K. Turoverov, *PLoS One*, 2014, **9**, e103878.

5. J. Luo, Z. Xie, J. W. Y. Lam, L. Cheng, H. Chen, C. Qiu, H. S. Kwok, X. Zhan, Y. Liu, D. Zhu and J. Luo, *Chem. Commun.*, 2001, **18**, 1740.

6. N. L. C. Leung, N. Xie, W. Yuan, Y. Liu, Q. Wu, Q. Peng, Q. Miao, J. W. Y. Lam and B. Z. Tang, *Chem. Eur. J.*, 2014, **20**, 15349–15353.

7. Z. Liu, B. Lyu, H. Lu, J. Tang, Q. Zhang, B. Jiao and Z. Liu, *Entomol. Gen.*, 2025, **45**, 25.

8. L. Shi, W. Yan, L. Sun, C. Hou, N. Wei, Z. Chen, J. Feng and L. Shi, *Pest Manag. Sci.*, 2022, **78**, 4407–4416.

9. R. Wang, S. Liu, F. S. Sun, X. Yu, X. Liu, B. X. Li, W. Mu, D. X. Zhang and F. Liu, *Chem. Eng. J.*, 2023, **455**, 140899.

10. X. Xu, X. Shi, P. Ding, B. Wang, M. Zeng, Y. Liu, Q. Wang and X. Xu, *Pest Manag. Sci.*, 2025, **81**, 4016–4026.

11. K. Zhao, G. Xu, L. Wang, T. Wu, X. Zhang, C. Zhang, Y. Zhao, Z. Li, Y. Gao and F. Du, *ACS Appl. Mater. Interfaces*, 2023, **15**, 37093–37106.

12. Z. Zhou, Y. Gao, G. Tang, Y. Tian, Y. Li, H. Wang, X. Li, X. Yu, Z. Zhang, Y. Li and Z. Zhou, *Chem. Eng. J.*, 2022, **446**, 137073.

Movie S1.

Under continuous stirring, the oil and aqueous phases were combined slowly, during which microspheres were visibly generated and progressively evolved.